Mon. Not. R. Astron. Soc. **000**, 000–000 (0000) Printed 19 December 2014 (MN LATEX style file v2.2)

Properties of barred spiral disks in hydrodynamical cosmological simulations

David Goz[1], Pierluigi Monaco[1,2], Giuseppe Murante[2], Anna Curir[3]
[1] *Dipartimento di Fisica - Sezione di Astronomia, Università di Trieste, via Tiepolo 11, I- 34131 Trieste – Italy (goz@oats.inaf.it)*
[2] *INAF, Osservatorio Astronomico di Trieste, Via Tiepolo 11, I-34131 Trieste – Italy (monaco, murante@oats.inaf.it)*
[3] *INAF, Osservatorio Astronomico di Torino, Strada Osservatorio 20, I-10025 Pino Torinese – Italy (curir@oato.inaf.it)*

arXiv:1412.2883v1 [astro-ph.GA] 9 Dec 2014

19 December 2014

ABSTRACT

We present a quantification of the properties of bars in two N-body+SPH cosmological simulations of spiral galaxies, named GA and AqC. The initial conditions were obtained using the zoom-in technique and represent two dark matter (DM) halos of $2-3\times10^{12}\,\mathrm{M}_\odot$, available at two different resolutions. The resulting galaxies are presented in the companion paper of Murante et al. (2014). We find that the GA galaxy has a bar of length 8.8 kpc, present at the two resolution levels even though with a slightly different strength. Classical bar signatures (e.g. pattern of streaming motions, high $m = 2$ Fourier mode with roughly constant phase) are consistently found at both resolutions. Though a close encounter with a merging satellite at $z \sim 0.6$ (mass ratio $1 : 50$) causes a strong, transient spiral pattern and some heating of the disk, we find that bar instability is due to secular process, caused by a low Toomre parameter $Q \lesssim 1$ due to accumulation of mass in the disk. The AqC galaxy has a slightly different history: it suffers a similar tidal disturbance due to a merging satellite at $z \sim 0.5$ but with a mass ratio of $1 : 32$, that triggers a bar in the high-resolution simulation, while at low resolution the merging is found to take place at a later time, so that both secular evolution and merging are plausible triggers for bar instability.

Key words: galaxies: formation - galaxies: structure - galaxies: kinematics and dynamics - methods:numerical

1 INTRODUCTION

The formation and evolution of structures within the Lambda Cold Dark Matter (ΛCDM) cosmological model is a very active and quickly evolving field. In this cosmological framework, galaxies form through cooling and condensation of baryons within dark matter halos (e.g., White & Rees 1978; Fall & Efstathiou 1980). The initial conditions are provided by cosmology, but the level of complexity of the problem is so high that following the evolution of galaxies is a great challenge. It is then convenient to address the problem using N-body hydrodynamical simulations. State-of-the-art hydrodynamical codes for the formation of galaxies include a treatment of the processes of radiative cooling, star formation, energy feedback from massive or dying stars, their chemical enrichment and, in some cases, accretion onto black holes and feedback from the resulting active galactic nuclei. Many of these processes take place on very small scales, compared with those that can be resolved by the simulation, so it is necessary to include them through suitable sub-resolution models. Thanks to recent progress, simulations are now able to produce galaxies with realistic morphologies, sizes and gas fractions. In particular, despite the relatively unsuccessful simulations shown in the Aquila comparison project (Scannapieco et al. 2012), the challenge of producing a disk galaxy in a Milky Way-sized halo with quiet merging history has been successfully carried out by several groups (e.g. Governato et al. 2007; Guedes et al. 2011; Marinacci et al. 2013; Stinson et al. 2013; Aumer et al. 2013).

One important observational aspect of disk galaxies is the presence of a bar: about 60 per cent of nearby disk galaxies are barred when observed in the near-infrared, while this figure lowers when galaxies are imaged in the optical (Eskridge et al. 2000; Barazza et al. 2008). Bars are believed to play a key role in the secular evolution of galaxy disks, particularly in the redistribution of angular momentum of baryonic and dark matter components (Debattista & Sellwood 1996, 2000). The non-circular motions of bars cause the migration of gas within the corotation radius towards the galaxy center, where it can give rise to a starburst or be accreted on a nuclear black hole. Also, the formation of a bar is believed to contribute to the formation of a disky or boxy/peanut bulge, often called pseudobulge (Kormendy 1982; Kormendy & Kennicutt 2004; Athanassoula 2005; Debattista et al. 2006).

The emergence of bars in simulated galaxy disks has been addressed in many papers, starting from the pioneering work of Ostriker & Peebles (1973) where stability of a disk-shaped rotating N-body system was obtained only in the presence of an ex-

© 0000 RAS

tended spherical halo. The origin of bars was ascribed to secular instabilities of massive disks (e.g. Efstathiou et al. 1982) or to tidal interactions and merging with galaxy satellites, that excite spiral structures or proper bars (e.g. Noguchi 1996; Dubinski et al. 2008). Sellwood et al. (1998) noticed that disk stability is influenced by the presence of a soft or hard center (namely a gently or steeply rising inner rotation curve), even when dark matter gives a negligible contribution to the inner part of the rotation curve.

More recent works addressed the effect of halo triaxiality (Curir & Mazzei 1999) and concentration (Athanassoula & Misiriotis 2002) on the growth of a bar in a disk hosted by an isolated halo with a Navarro et al. (1996) profile. In these works the initial conditions represent an equilibrium configuration of a disk embedded in a dark matter halo; this setting is suitable to study bar formation in the absence of further external perturbations. Halo triaxiality was reported by Curir & Mazzei (1999) to be a trigger of bar formation, while Athanassoula & Misiriotis (2002) found that the bar strength correlates with halo concentration.

The study of bar formation in cosmological halos has been faced in two ways. Curir et al. (2006) built zoomed Initial Conditions (hereafter ICs) of DM halos in cosmological volumes, let them evolve with an N-body code and placed model disks inside the halos that were present at some specified redshift. That paper considered purely stellar disks, while stellar+gas disks were presented in Curir et al. (2007) and the effect of star formation was considered in Curir et al. (2008). In these works it was shown that halo triaxiality, at the level commonly found in simulated DM halos, triggers the formation of bars. The presence of gas leads to the destruction of the bar after a few dynamical times if the disk gas fraction is higher than ~ 20 per cent, but the switching on of star formation inhibits this destruction. Different conclusions were reached by Berentzen et al. (2006), who noticed that the formation of a bar was weaker in halos with higher triaxiality. Athanassoula et al. (2013) showed the complex influence of halo triaxiality on the bar strength: at earlier times it triggers an instability while, at later times when secular evolution takes place, it has a stabilizing effect.

The second way of studying bar formation consists in addressing the emergence of bars in fully cosmological simulations of the formation of spiral galaxies (Scannapieco & Athanassoula 2012; Kraljic et al. 2012; Okamoto 2013; Guedes et al. 2013; Okamoto et al. 2014). The obvious advantage of this approach, of a much more realistic representation of gravitational forces within a non idealized DM halo, is balanced by the difficulty in obtaining a realistic disk galaxy in this context. In particular, extended disks with flat rotation curves are obtained only when efficient feedback from star formation is present, but too strong feedback can lead to the destruction of the disk (Scannapieco et al. 2012). This is where the sub-resolution modeling of stellar feedback becomes crucial.

Scannapieco & Athanassoula (2012), using the version of GADGET (Springel 2005) described in Scannapieco et al. (2006), found long and strong bars in two simulated galaxies; in particular the strengths, lengths and projected density profiles of the bars were found within the range of values given in the observations of Gadotti (2011). Kraljic et al. (2012), using the Eulerian code RAMSES (Teyssier 2002), studied the evolution of galactic bars in a sample of 33 zoomed-in cosmological halos. They found that after $z \approx 1$ almost 80% of spirals galaxies host bars and they suggested that the epoch of bar formation starts from the late "secular" phase and contributes to the growth of pseudobulges, even if the bulge mass budget remains dominated by the contribution of mergers. Furthermore, most of the bars formed at $z \lesssim 1$ persists up to $z = 0$, while early bars at $z > 1$ often disappear and reform several times. Okamoto (2013) analyzed two simulations of disk galaxies with disky pseudobulges (Sersic index < 2), one of which presents a strong bar and a "boxy bulge". They concluded that, at variance with the standard picture, the main channel of pseudobulge formation is high-redshift starbursts and not the secular evolution of the disk, although this contributes to it in a non-negligible way. Guedes et al. (2013) used their Eris simulation to investigate the interplay between a stellar bar and the formation and evolution of a pseudobulge. They found, again at variance with the standard picture, that the bulk of mass in their pseudobulge forms early ($z \sim 4$), fast (~ 2 Gyr) and in situ, starting from a bar instability triggered by tidal interactions with a passing satellite. The bar is destroyed ($z \sim 3$) by several minor mergers, then reforms later ($z \sim 2$), again triggered by tidal interactions, but the redistribution of angular momentum within stars and gas, driven to the center by the bar itself at $z \sim 1$, leads to the gradual breakup of the bar structure. Very recently Okamoto et al. (2014) studied the evolution of two bars formed in cosmological Milky Way-sized halos. As commonly found in idealized simulations, the rotation speed of the stronger bar was found to decrease with time by transferring its angular momentum to the dark matter halo, while other behaviours, such as oscillations of pattern speed, were more peculiar to the cosmological case. The weaker bar was found to slow down, while its amplitude was staying constant. The authors pointed out that the main difference between idealized and cosmological simulations is the inclusion of energy and mass released from stellar populations, which leads to a different central density structure.

In Murante et al. (2014) (hereafter paper I) we present simulations of Milky Way-sized DM halos performed with the Tree-PM+SPH code GADGET3 (Springel 2005), where star formation and stellar feedback are treated with the sub-resolution model, named MUlti-Phase Particle Integrator (hereafter MUPPI), presented in Murante et al. (2010). These simulations follow the chemical enrichment of the Inter-Stellar Medium (ISM) and its metal-dependent radiative cooling using the model of Tornatore et al. (2007) and Wiersma et al. (2009). The two sets of initial conditions for the simulations, the GA set by Stoehr et al. (2002) and the AqC set of Scannapieco et al. (2006), are available at different refinement levels and they were used to study the stability of results with resolution. The resulting galaxies are shown in paper I to resemble observed spirals in many regards; in particular, the resulting disks are extended, with small bulges ($B/T \sim 0.2$) and flat rotation curves. As shown in that paper, at $z = 0$ both spiral galaxies hosted by the two halos show an extended bar and this feature is clearly visible at two resolutions both in GA and AqC sets.

In this paper we quantify the properties and kinematics of the bars of the GA and AqC galaxies of paper I. We find that, in the GA case and during the development of the instability ($z \leqslant 0.3$), bar properties and time evolution are very similar at the two resolutions, while in the AqC case some differences are noticed that can be ascribed to the different orbits and timing of a minor merger at the two resolutions.

This is, to our knowledge, the first time that, in a cosmological simulation, a bar instability is found to develop in such a similar way at different resolutions. This prompts us to consider these bars as due to physical and not to numerical processes and to study the trigger of this instability, investigating the role of secular evolution and minor mergers.

The paper is organized as follows. Section 2 gives a brief account of the simulations used in this paper. Section 3 presents a complete quantification of stellar orbits and bar strength and length

in the GA galaxies, addressing the question of the physical cause of the bar and the time at which it appears. Section 4 shows results for the AqC galaxies, highlighting the differences with the GA simulations and investigating the physical origin of such differences. Finally, Section 5 gives a summary and conclusions.

2 SIMULATIONS

Simulations were performed using the GADGET3 code (Springel 2005), where gravity is solved with a Tree code, aided by a Particle Mesh scheme at large scales, while hydrodynamics is integrated with an SPH solver that uses an explicitly entropy-conserving formulation with force symmetrization (Springel 2005). Star formation and feedback are performed with MUPPI (Murante et al. 2010), an effective model that attempts to take into account the structure of the ISM at unresolved scales by assuming that each gas particle, at sufficiently high density, is made up of a cold and a hot phase in thermal pressure equilibrium, plus a virtual stellar component. Energy from feedback is distributed to neighbouring particles both in the form of thermal and kinetic energy, as described in paper I and in Murante et al. (2010). Chemical evolution and tracking of 11 elements is performed with the code of Tornatore et al. (2007), while metal-dependent cooling is performed following Wiersma et al. (2009). A full description of the code is given in the companion paper of paper I, we refer to this paper for all details.

The two sets of initial conditions that we used are resimulations of DM halos of mass $\sim 3 \times 10^{12}$ M$_\odot$ (GA) and $\sim 2 \times 10^{12}$ M$_\odot$ (AqC), with quiet merger history since $z \sim 2$ so as to avoid the risk of late-time major mergers that can severely damage or destroy the disks. In particular, the AqC is part of the Aquarius series (Springel et al. 2008) of eight halos, used by Scannapieco et al. (2009) to study the formation of disk galaxies; it was chosen because it was giving the lowest bulge-over-total (B/T) ratio in that paper. Its level 6 and 5 resolutions were used in the Aquila comparison project (Scannapieco et al. 2012), in which we participated with an early version of our code with primordial cooling and purely thermal feedback. As a matter of fact, both galaxies happen to suffer a minor merger of mass ratio of order $1:50$ (GA) and $1:30$ (AqC) at $z \sim 0.5$. For both sets of ICs we use two resolution levels with initial gas particle masses of $\sim 2 \times 10^6$ M$_\odot$ (GA1 and AqC6) and $\sim 3 \times 10^5$ M$_\odot$ (GA2 and AqC5). Plummer-equivalent softening at $z < 6$ is set, for the two resolutions, to 0.65 and 0.325 kpc/h in physical coordinates, at higher redshift we keep it fixed in comoving coordinates.

Table1 reports the main properties of the four sets of ICs, together with the main properties of their central galaxies at $z = 0$. Simulations were post-processed with a standard Friends-of-Friends (FoF) algorithm to select the main halo of the high-resolution region and with the substructure-finding code SubFind (Springel et al. 2001). We assumed that the particles that constitute the galaxy are stars and cold ($T < 10^5$ K) or multi-phase gas particles, hereafter called "galaxy particles". The galaxy was first identified as the object laying within $1/10$ of the virial radius r_{200}, centered on the center of mass of the FoF halo, then the galaxy position was refined by computing the center of mass of galaxy particles lying within 8 kpc (a distance at which it is unlikely to find satellite galaxies) and by iterating the computation with the new center until convergence within 1 pc was reached. We checked that this position is very similar to the center of the main substructure of the FoF halo, computed by SubFind using the position of the most bound particle. The reference frame was then aligned with the inertia tensor of galaxy particles, with the Z-axis[1] along the eigenvector corresponding to the largest eigenvalue and in the direction so as to have a positive scalar product with the angular momentum; the other two axes were aligned with the other eigenvectors so as to preserve the property $\hat{X} \times \hat{Y} = \hat{Z}$. We checked that, whenever a significant disk is present, the angular momentum of the galaxy particles within $r_{200}/10$ is always very well aligned, within less than one degree, with the Z-axis.

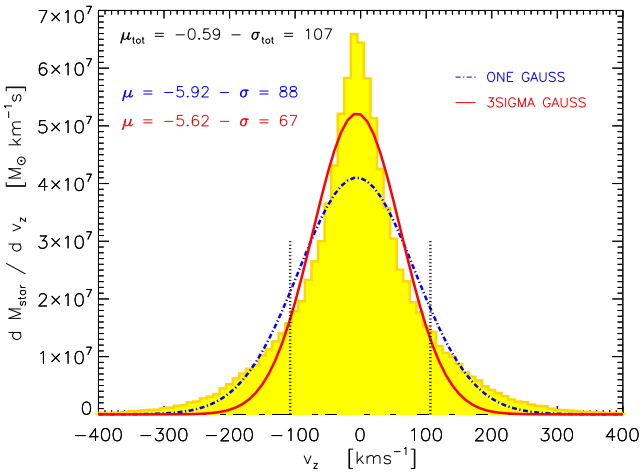

Figure 2. Mass-weighted histogram of stellar velocities for GA2 in the radial bin from 3 to 4 kpc for the GA2 galaxy at $z = 0$. Measured average and r.m.s are $\mu_{tot} = -0.59$ km/s and $\sigma_{tot} = 107$ km/s, the r.m.s. is denoted by two dotted black vertical lines. The resulting fits (top left of the panel) for averages and dispersion with the Gaussian fit (dot-dashed blue line) and 3-σ rejection (continuous red line) methods are reported in the figure with the same color as the corresponding line, in km/s.

3 THE GA1 AND GA2 GALAXIES

In this Section, we study the GA galaxies obtained at the two resolution levels, GA1 (lower resolution) and GA2 (higher resolution). We show both simulations to address the stability of our result with respect to resolution.

3.1 The vertical structure of the disk

The relatively high values of the force softening used in these simulations do not allow us to resolve the vertical structure of the stellar thin disk. Nevertheless the kinematic state of the disk is relevant in the study of disk instabilities, as it is well known that a hot disk is more stable (see, e.g., the analysis based on the Toomre parameter presented below). From this point of view, it is a better choice to address the distribution of stellar velocities in place of stellar positions. Indeed, the force exhorted by a planar distribution of mass depends mostly on its mass surface density, a quantity that is independent of disk scale height, so we expect the velocity dispersion of stars to be more convergent with resolution than the scale height

[1] In this paper we use the small letter z to denote redshift and the capital letter Z to denote the spatial vertical axis.

Simulation	$\epsilon_{\rm Pl}$ (kpc/h)	M_{gas} ($M_\odot$/h)	M_{star} ($M_\odot$/h)	N_{star}	$r_{200}/10$ (kpc)	M_{bulge} ($M_\odot$)	M_{disk} ($M_\odot$)	B/T
GA2	0.325	$3.0 \cdot 10^5$	$7.5 \cdot 10^4$	1154243	29.98	$1.4 \cdot 10^{10}$	$8.8 \cdot 10^{10}$	0.20
GA1	0.65	$2.8 \cdot 10^6$	$7.0 \cdot 10^5$	146196	30.37	$2.0 \cdot 10^{10}$	$1.1 \cdot 10^{11}$	0.22
AqC5	0.325	$3.0 \cdot 10^5$	$7.5 \cdot 10^4$	803889	23.82	$1.1 \cdot 10^{10}$	$5.7 \cdot 10^{10}$	0.23
AqC6	0.65	$2.4 \cdot 10^6$	$6.0 \cdot 10^5$	111989	24.15	$1.4 \cdot 10^{10}$	$6.3 \cdot 10^{10}$	0.24

Table 1. Basic characteristics of the different simulations. Column 1: simulation name; column 2: Plummer-equivalent softening length for gravitational forces, fixed in physical coordinates below $z = 6$ and in comoving coordinates at higher redshift; column 3: mass of the gas particles; column 4: mass of the star particles; column 5: number of star particles within $r_{200}/10$; column 6: virial radius $r_{200}/10$; column 7: stellar bulge mass at $z = 0$; column 8: stellar disk mass at $z = 0$; column 9: bulge-over-total stellar mass ratio at $z = 0$;

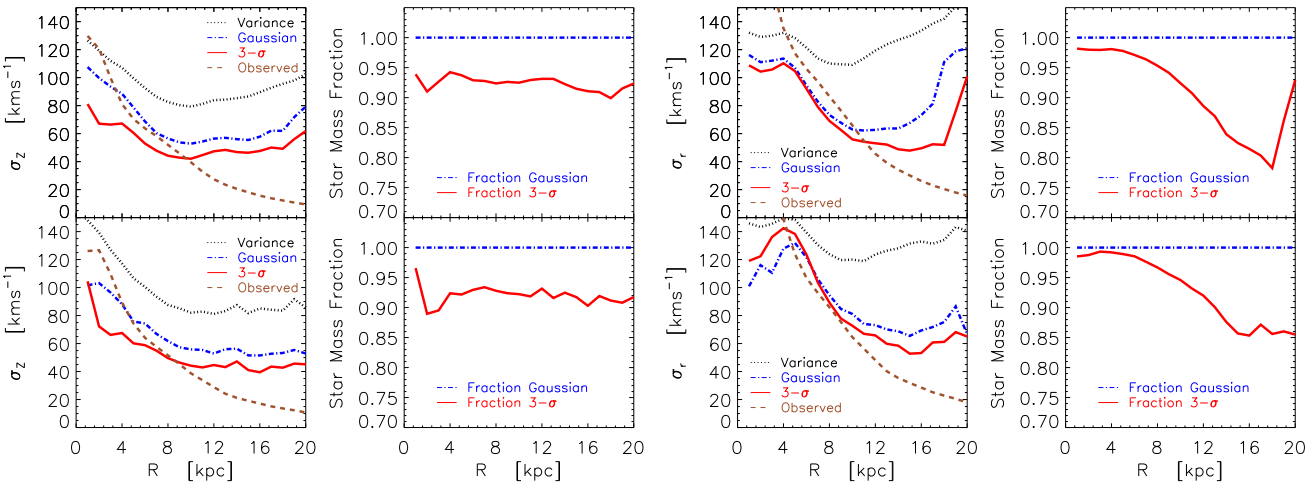

Figure 1. Vertical velocity dispersion σ_Z and σ_r, and fractions of mass used to compute the relative dispersion; the variance and Gaussian fit methods use all particles, so for these the latter quantity is unity, while the $3-\sigma$ rejection method excludes particles with large velocities and in this case the latter quantity gives the fraction of mass that has not been excluded. The upper figures give results for GA2, the lower figures for GA1. The left pair of panels gives results for σ_Z, the right pair for σ_r. Dotted black, dot-dashed blue, continuous red and dashed brown lines give respectively the r.m.s, Gaussian, $3-\sigma$ rejection and observation-oriented estimates of velocity dispersion.

itself. Below, we compute the velocity dispersion both in the vertical, Z-direction and in the radial, r-direction. The latter enters in the Toomre stability criterion.

To compute stellar velocity dispersion, we use all stars within $r_{200}/10$ from the center, so at each polar radius we will have a mix of stars from the disk and from the stellar halo[2]. Assuming that the thin disk is the most massive component and that its vertical or radial velocities are roughly Gaussian distributed, the (mass-weighted) variance of disk stars will be severely affected by the minor component with a higher velocity dispersion. Figure 1 shows, for both GA2 (upper panels) and GA1 (lower panels), the mass-weighted root mean square (hereafter r.m.s.) of vertical (left panels) and radial (right panels) velocity dispersion of all stars as black lines. Figure 2 reports, for the radial bin from 3 to 4 kpc, the mass-weighted histogram of vertical velocities in which black vertical lines mark the r.m.s. of the distribution, that is clearly not representative of the width of the main component.

To improve this measure we tested two options: a Gaussian fit of the distribution of velocities in each bin of polar radius (blue lines in the two Figures) and a Gaussian fit with recursive rejection of $> 3-\sigma$ interlopers, performed until convergence is reached (red lines in the two Figures). Since the $3-\sigma$ rejection method implies that some mass is discarded, in Figure 1 we report on the right of velocity profiles the fraction of mass that is used to compute them, as a function of radial distance. The Gaussian fit method uses all the mass, so it is reported as a line at unity. It can be noticed that, for both velocity components, the Gaussian fit method gives significantly lower velocity dispersion, while a further suppression is obtained with the $3-\sigma$ rejection method. The predicted distributions are shown in Figure 2, again as blue and red lines. From this figure, it is apparent that the $3-\sigma$ rejection method gives the most faithful representation of the width of the main mass component, at the modest cost of excluding less than 10 per cent of mass in the case of vertical velocity dispersion σ_Z and an amount ranging from 1-2 per cent at small radii to $\sim$20 per cent at large distances in the case of the radial velocity dispersion σ_r. We also tried to fit the velocity distributions with two Gaussians, but the results were unstable and not satisfactory and for this reason we dropped this method.

In Figure 1 we also compare these estimates of σ_Z and σ_r with observation-oriented estimates. We follow Leroy et al. (2008) who computed the Toomre Q parameter for the THINGS sample of local galaxies. Since direct measurements of stellar velocity dispersion are *"extremely scarce"*, in their Appendix B they assumed that the stellar scale height $h_\star$ is constant throughout the disk, that this same quantity is related to the disk scale radius $r_\star$ through the

[2] We may have some contribution from a thick disk component, whose study is however hampered by the relatively poor softening that we use and is anyway beyond the interests of the present paper.

observed relation $h_\star = r_\star/7.3$ and that stars are isothermal in the Z-direction. As a result:

$$\sigma_Z = \sqrt{\Sigma_\star \frac{2\pi G r_\star}{7.3}}\,, \quad (1)$$

where $\Sigma_\star$ is the disk stellar surface density. For the radial velocity dispersion, the same authors assumed that $0.6\sigma_r = \sigma_Z$. For the GA1 and GA2 disks we use a disk scale length $r_* = 3.93$ and 4.45 kpc, estimated in paper I by fitting the radial profile of stellar mass surface density. These estimates are shown in the Figure 1 as brown lines. As a result, at $r < 10$ kpc both the Gaussian and the $3-\sigma$ rejection methods yield velocity dispersions that are broadly compatible with those that would be expected in an observed galaxy. In more detail, GA1 shows a marginally hotter disk, especially as far as radial motions are concerned, but these are influenced by the radial streaming motions due to the bar itself, that will be quantified below. The outer parts of the disk are significantly hotter than this estimate, but we know that, at large distances, disk scale lengths start to increase, so this discrepancy could be not very significant.

This analysis demonstrates that, despite the relatively large softenings used, the kinematic state of our disks is compatible with observational evidence, at least in the inner regions that are subject to bar instability. However, we know that these velocity dispersions are severely affected by numerics and the marginally hotter GA1 disk clearly supports this warning. In paper I, we present results of simulations of the GA1 obtained with different softenings and we show that, while lower values of the softening result in higher stellar velocity dispersion (simply measured there as r.m.s.), convergence is not yet fully achieved for the value of softening used here. Therefore these velocities are very likely influenced by 2-body scattering of star particles, but this influence does not lead to unrealistic thickening of the disk.

3.2 Morphology and circularities

Extended density maps of the two galaxies are given in paper I. Figure 3 shows maps of stellar mass surface density for the central part of the two simulated galaxies at redshift 0. Each map spans ± 12.5 kpc in each dimension. The figure shows, on the upper panels, the maps of the GA2 simulation in the XY-, XZ- and YZ-plane, while the lower panels show the same maps for the GA1 simulation. The color coding represents the Log surface density and values are given in the color bar. The maps were obtained by projecting all star particles within $r_{200}/10$ and smoothing the resulting surface densities on a grid, whose pixel is set equal to the softening length in both cases. We find that in both simulations the isodensity contours in the face-on map are not round but present a flattened structure; the bar is aligned along the X-axis. The edge-on maps sample the bar along its long (XZ projection) and short (YZ projection) axes and, as expected, the isodensity contours are flatter when the disk particle distribution is seen along the major bar axis.

The circularity of a star particle is usually defined as the ratio of the z-component of its specific angular momentum, $j_z = r v_{\rm tan}$ (where $v_{\rm tan}$ is the tangential velocity in a cylindrical coordinate system) and the angular momentum of a reference circular orbit. Two methods have been proposed to compute this reference angular momentum. Scannapieco et al. (2009) and other authors used the angular momentum of a circular orbit at the same radius, $j_{\rm circ} = r\sqrt{GM(<r)/r}$, while Abadi et al. (2003) proposed to use $J_{\rm max}(E)$, the maximum specific angular momentum possible given the binding energy of the particle E. This second definition constrains circularity to be < 1. As in paper I, in this paper we use the first definition, so that:

$$\epsilon = j_Z / j_{\rm circ} \quad (2)$$

However, we also tested the second definition at $z = 0$ and found the same qualitative features of the circularity diagrams obtained with Equation 2.

In Figure 4 we show 2D histograms of circularities as a function of polar radius r along the galaxy disks, for both galaxies at six different times. We expect a disk to be visible as a narrow distribution around $\epsilon \sim 1$, while a component scattering around $\epsilon \sim 0$ will be identified as a bulge or a spherical halo, depending on r. The 2D histograms are shown as a map of mass per unit bin size (kpc and circularity in the two dimensions), with isodensity contours showing the preferential locus of star particles. For each row, the upper and lower panels give the histogram for GA2 and GA1 respectively. Starting from the upper left panels, the two rows show results for $z = 1.5$, 1, 0.7, 0.5, 0.2, 0. These times are chosen to follow the main phases of the formation of the bar, as it will be explained below. This figure allows us to monitor the formation of the disk in the two simulations. The first point that is worth noting is that the circularity histograms are notably independent of resolution, so we will describe GA1 and GA2 together. At $z = 1.5$ the galaxy is mostly a spheroid, while a disk has started to form at $r < 6kpc$. A clear and thin disk structure is visible at $z = 1$. The structure is broader at $z < 0.6$, where tidal interactions with a satellite of mass $M_\star = 1.2 \times 10^9$ M$_\odot$, that culminate with a minor merger at $z = 0.35$, are heating the disk. Beyond $z = 0.2$, the region at intermediate circularities, $\epsilon \sim 0.5$ and at $1 < r < 5$ kpc, starts to be populated, especially for the GA1 galaxy. Because stars in the bar have large systematic radial motions, this is a sign of the emergence of a bar structure.

The fraction of stellar mass as a function of circularity, i.e the projection in radius of the circularity histograms of Figure 4, is shown in figure 3 of paper I for $z = 0$. There a simple, kinematically-based decomposition (that loosely follows Scannapieco et al. 2008) is used to compute the stellar B/T. We assume that counter-rotating star particles ($\epsilon < 0$) within $r_{200}/10$ constitute half of the spheroidal component, so the bulge mass is computed as twice the mass of these counter-rotating stars. B/T was then computed as:

$$B/T = M_{\rm bulge}/(M_{\rm bulge} + M_{\rm disk}) \quad (3)$$

B/T values at $z = 0$ are reported in Table 1.

3.3 Kinematics of the central region

Here we quantify the kinematics of the central region of the galaxy, that hosts both bar and bulge. It will be demonstrated in Section 3.5 that in GA1 as well as in GA2 a bar appears only towards the end of the simulation, starting from $z = 0.2$, so we analyze here only the galaxy at $z = 0$.

As suggested by Okamoto (2013), the expected kinematic signature of a bar is a higher value of line-of-sight velocities with respect to vertical ones. We repeat the analysis suggested in that paper in Figure 5, that shows velocity dispersion σ_{los} of stars along the "line of sight" (the Y axis in the density maps; red lines in the figure) and along the vertical direction σ_Z (Z axis; blue lines in the

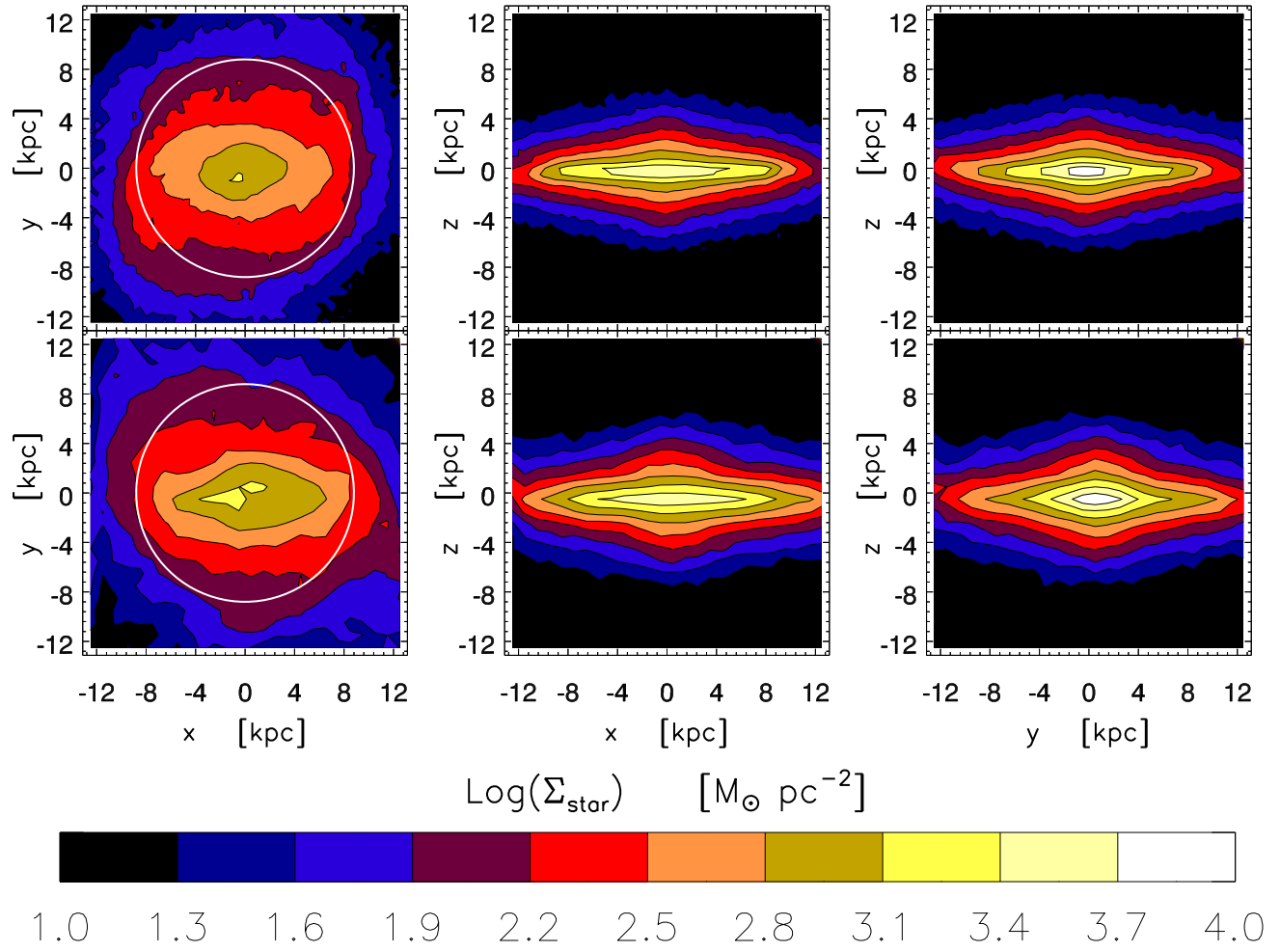

Figure 3. Projected stellar maps of the GA2 (upper panels) and GA1 (lower panels) galaxies at $z = 0$ in boxes centered on the galaxy that extend 25 kpc across. Color coding follows the Log of stellar mass surface density as indicated by the color bar. The three columns show projections in the face-on XY-plane (left), edge-on XZ-plane (middle) and edge-on YZ-plane (right). The white circle marks the bar length $L_{\rm bar}$.

figure). Velocity dispersions were computed with the 3-σ rejection method explained in Section 3.1.

We find that, while vertical velocity dispersion gets values of $\sim 50-60$ km/s with a very flat dependence on distance from the center, radial velocity dispersion takes higher values. In the GA2 case, radial velocities peak at ~ 100 km/s, twice the vertical ones, while in the GA1 case an even higher peak (130 km/s) is present. In both cases, a small dip at the galaxy center is present.

A pronounced, radial streaming pattern is expected in non-axisymmetric potentials like that of a stellar bar (e.g. Bosma 1978). Figure 6 shows 2D maps, in the face-on XY plane, of average radial velocities computed on the same box size and grid as in Figure 3. To minimize contamination from halo motions, median velocities are computed only for stars lying within 1 kpc from the midplane. As shown in the color bar below, blue/black colors denote negative velocities, while yellow/while colors denote positive velocities. A symmetric and squared pattern of streaming motions is evident in both cases, with higher velocities for the GA1 galaxy. At larger distances from the center, the velocity pattern connected to the spiral arms is very visible for GA2. We conclude that the kinematics of stars in the inner regions of these galaxies is dominated by streaming motions as expected.

3.4 Quantification of bar strength and length

We quantify the strength of the bar following the analysis of Scannapieco & Athanassoula (2012) and Kraljic et al. (2012). This is based on the Fourier transform of the surface density of the disk:

$$\Sigma\left(r,\theta\right) = \frac{a_0(r)}{2} + \sum_{n=1}^{\infty}\left[a_n(r)\cos(n\theta) + b_n(r)\sin(n\theta)\right] \quad (4)$$

where r is the polar radius and θ the azimuthal position on the disk plane. To perform the transform, particles are radially binned and the following coefficients are computed for each bin:

$$a_n(r) = \frac{1}{\pi}\int_0^{2\pi}\Sigma(r)\cos(n\theta)d\theta\,,(n\geqslant 0) \quad (5)$$

$$b_n(r) = \frac{1}{\pi}\int_0^{2\pi}\Sigma(r)\sin(n\theta)d\theta\,,(n>0) \quad (6)$$

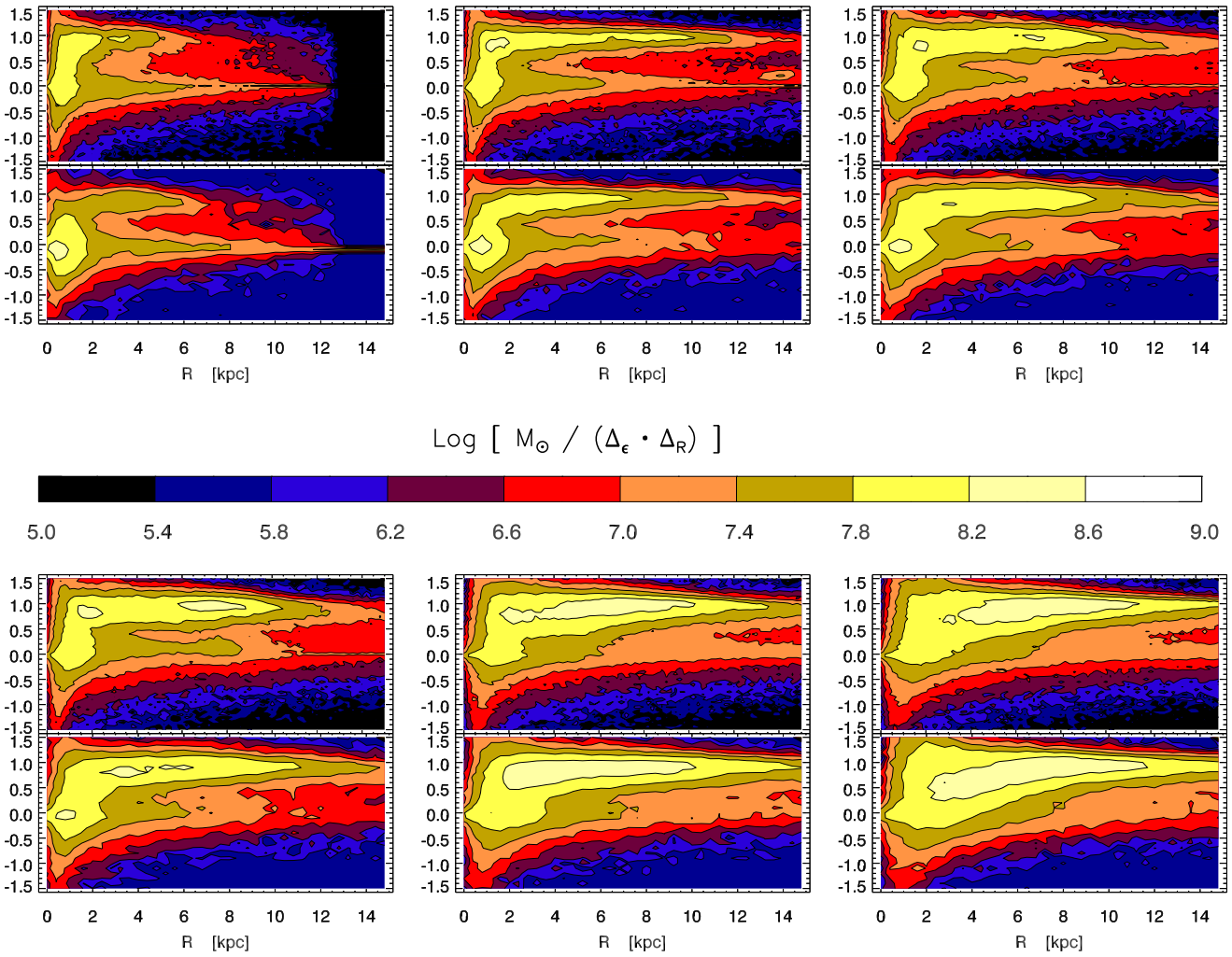

Figure 4. 2D histograms of circularity (Eq. 2) and polar radius, at six different times. In each panel, color coding refers to the Log of stellar mass per unit bin area as indicated by the color bar, the black lines are the corresponding isodensity contours. Each pair of panels gives results for the GA2 (upper panels) and GA1 (lower panels) galaxies. From the upper left panels, redshifts are $z = 1.5, 1, 0.7, 0.5, 0.2, 0$.

where Σ is the surface density of the stellar disk. The Fourier amplitude of each mode is defined as:

$$C_n(r) = \sqrt{a_n^2(r) + b_n^2(r)}\,, \quad C_0(r) = a_0(r)/2 \qquad (7)$$

The presence of a bar is revealed by a significant value of the C_2 component, that is higher than even components of further order.

In Figure 7 we show the amplitudes of the first four even components, normalized to the $n = 0$ one, C_n/C_0. In both cases the C_2 component is significantly higher than the other components; for the GA2 it peaks at a value of 0.4 at 6 kpc, with a broad plateau starting from 2 kpc. GA1 shows a narrower plateau between 5 and 7 kpc, reaching a higher value of 0.7. This confirms that, consistently with the higher radial velocities, the bar in the GA1 simulation is stronger than in GA2. Higher order moments show smaller and smaller values in both cases; they peak at different scales and this is a sign that the bar is not perfectly symmetric. We also checked that odd modes have small values and this is again consistent with what we expect from a bar.

These results are broadly consistent with observations that show a variety of radial Fourier profiles of bars, ranging from simple symmetric profiles, that can be represented by two overlapping Gaussian components, to more complex curves. Since C_n/C_0 value spans between 0.4 and 0.8 (Elmegreen & Elmegreen 1985; Ohta et al. 1990; Ohta 1996; Aguerri et al. 1998, 2003; Buta et al. 2006), both GA galaxies would be classified as barred. Moreover, the amplitudes of GA2 show relatively high values also at large radii, where the signature of streaming motions (Figure 6) is already lost but prominent spiral arms are present. This shows a limit of the analysis based simply on Fourier amplitudes, where spiral arms give weak signatures that can be confused with those of bars.

To evaluate the length of the bar, among many published methods (e.g. Combes & Elmegreen 1993; Debattista & Sellwood 2000; Michel-Dansac & Wozniak 2006), we use the one proposed by Athanassoula & Misiriotis (2002). This is based on the fact that, for an ideal bar, the phase of the $m = 2$ mode should be constant as long as the probed scale is within the bar, while beyond it the phase is expected to fluctuate due to spiral arms. We implement this method by calculating, for each radial bin, the phase Φ of the $m = 2$ mode as:

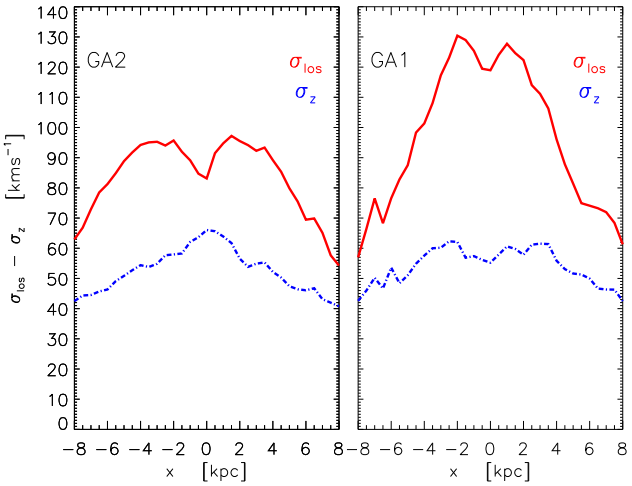

Figure 5. Profiles of line-of-sight velocity dispersion σ_{los} (continuous red lines) and vertical velocity dispersion σ_Z (dot-dashed blue lines) of stars at $z = 0$, when the galaxy is observed edge-on in the direction perpendicular to the bar main axis. Left and right panels show GA2 and GA1.

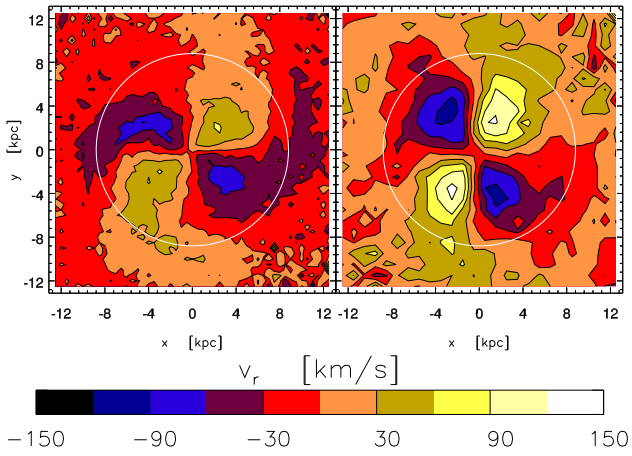

Figure 6. Radial velocity maps on face-on views (XY projection) of the two simulated GA2 (left panel) and GA1 (right panel) galaxies. The boxes are 25 kpc across. Color coding follows the median radial velocity of stars within 1 kpc from the midplane, as indicated by the color bar. The white circle marks the bar length $L_{\rm bar}$.

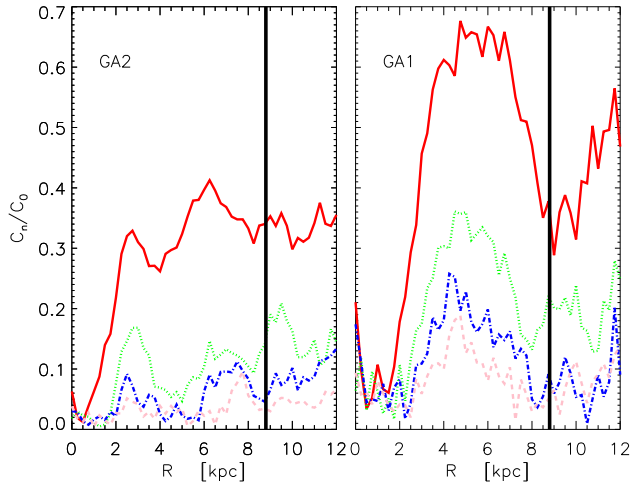

Figure 7. Fourier amplitudes C_n/C_0 for even components $n = 2$ (continuous red line), $n = 4$ (dotted green line), $n = 6$ (dot-dashed blue line), $n = 8$ (dashed pink line) for stars of GA2 (left panel) and GA1 (right panel). The black lines mark the bar length $L_{\rm bar}$ kpc.

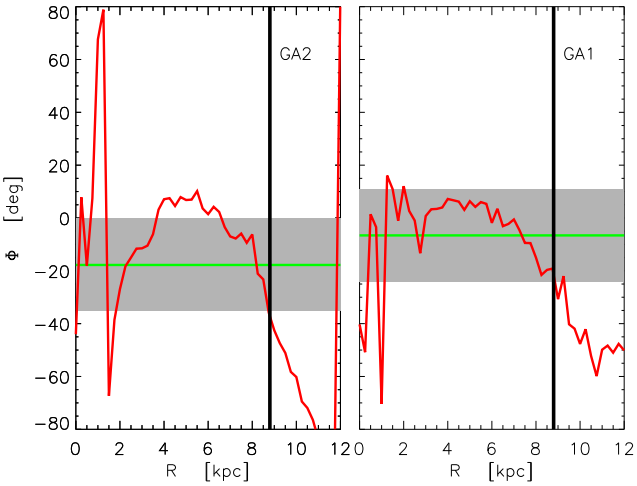

Figure 8. Phase of stellar distribution for GA2 (left panel) and GA1 (right panel). Red lines report the phase Φ of the $n = 2$ mode as a function of radius, the green horizontal line marks the overall phase $\Phi_{\rm disk}$ of the disk within 12.5 kpc. The shaded area gives the allowed range of $\Phi_{\rm disk} \pm \arcsin(0.3)$. The black lines correspond to the bar length $L_{\rm bar}$.

$$\Phi(r) = \arctan\left(b_2(r)/a_2(r)\right) \quad (8)$$

The average phase is computed applying Equations 5 and 6 to all star particles with $r < 12.5$ kpc, then computing $\Phi_{\rm disk}$ as in Equation 8. The result is reported in Figure 8 as a red line, while the green one corresponds to the average phase. The bar length is defined as the largest radius where these two last quantities differ less than a certain value. As discussed in Athanassoula & Misiriotis (2002), the choice of the constant is somehow arbitrary. In that paper the authors suggested a range of $\pm\arcsin(0.3)$, while tighter ranges were used by other authors (e.g. Kraljic et al. (2012) used $\pm\arcsin(0.1)$). We will demonstrate below that the GA2 bar is a caught in an early development phase and it is still weak, so we adopt the more permissive criterion of $\pm\arcsin(0.3)$. For both GA2 (left panel) and GA1 (right panel) the phase fluctuates in the inner 1-2 kpc, then is relatively stable for several kpc and goes out of the shaded region at 8.8 kpc in both cases. It must be noticed that the phase of GA2 gets marginally above the shaded region from 4 to 6 kpc, but given the arbitrariness of the used value we neglect this minor issue. We then take $L_{\rm bar} = 8.8$ kpc as a measure of bar length (see the vertical black line in the Figure) and notice that it is remarkably independent of resolution.

Another possible method proposed by Athanassoula & Misiriotis (2002) to evaluate bar length is based on the scale at which the Fourier coefficient C_2/C_0 goes to zero. Indeed, for an ideal bar on an axisymmetric disk, we would expect this coefficient to show a plateau and then drop

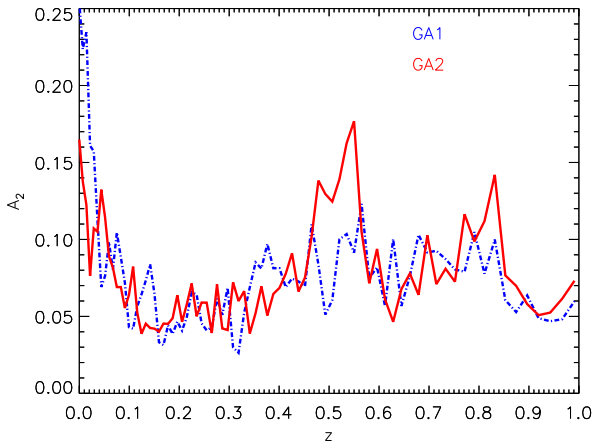

Figure 9. Relative mode strength A_2 as a function of redshift for the GA1 (dot-dashed blue) and GA2 (continuous red) galaxies, starting from $z = 1$.

quickly beyond the bar. In a more realistic context one should define a threshold with respect to the maximum and define the bar length as the radius at which the amplitude of the Fourier mode gets below it. In Figure 7 the vertical black lines denote the bar length as estimated by the phase method. In the GA1 case, using a drop of the coefficient by a factor of two, it would give almost the same bar length, while, as noticed above, in the GA2 case the spiral pattern gives a signal comparable to that of the bar. $L_{\rm bar}$ is reported as a circle also in Figures 3 and 6 and in both cases the estimated bar length separates the inner region, dominated by flattened isodensity contours and streaming motions, from the outer region dominated by spiral arms. We conclude that the phase method gives a fair estimate of $L_{\rm bar}$.

We can compare our results with $\sim$ 300 observed galaxies presented in Gadotti (2011); our $L_{\rm bar}$ value is at the high end of the distribution given in this observational work, but well compatible with it.

3.5 The origin of bar instability

To estimate the time at which the bar is triggered, we quantify how bar strength grows by computing the so-called relative mode strength A_2. This is the ratio of the integrals, weighted by area, of the coefficients C_2 and C_0 over the bar length $L_{\rm bar}$, taking into account its value estimated by the previous method in Section 3.4.

$$A_2 = \frac{\int_0^{L_{\rm bar}} C_2(R) R dR}{\int_0^{L_{\rm bar}} C_0(R) R dR} \qquad (9)$$

We perform this calculation for all simulation outputs since $z = 1$, when the disk is still young and both GA1 and GA2 show no sign of a bar. Figure 9 shows the evolution of A_2 with redshift for GA2 (red line) and GA1 (blue line). At $z < 0.7$, two different episodes of growth of A_2 are visible at z from 0.6 to 0.45 (at least for GA2) and at $z < 0.2$. The episode at $z \sim 0.5$ is due to a minor merger already mentioned above. A satellite of stellar mass 1.25×10^9 M$_\odot$ in GA2 and 1.35×10^9 M$_\odot$ in GA1 performs close orbits around the main galaxy. For GA2, the closest encounter is found at $z = 0.57$, where the distance of the satellite from the galaxy center is 12 kpc. The stellar mass ratio is $1 : 50$ at the beginning of the interaction, slowly decreasing because of the continuous growth of the stellar mass of the central galaxy. Two more close encounters are found before the satellite is tidally disrupted into the halo of the main galaxy ($z = 0.35$). These interactions trigger non-axisymmetric perturbations, so that GA2 acquires A_2 values equivalent to those at $z = 0$. During this period the disk is noticeably disturbed and a bar-like morphology is visible only in one output (the time interval between outputs being $\sim$ 100 Myr). In Figure 10 we show in the left panel a face-on density map of GA2 at $z = 0.55$ (just after the nearest encounter), analogous to Figure 3, and in the right panels the C_2/C_0 and phase diagrams, analogous to Figures 7 and 8. While disk morphology is clearly disturbed, the C_2 coefficient takes on significant values especially at large radii, while the phase analysis reveals that the structure does not behave as a bar. So the high value of A_2 is determined by the outer spiral arms more than by a central bar. This transient lasts from the first near passage of the satellite to its destruction, $\sim$ 700 Myr in total, corresponding to $\sim 3-4$ revolutions of the disk. Then the A_2 coefficient quickly returns to ~ 0.1 and keeps decreasing slowly with time.

The history of GA1 is similar. In this case the satellite is never found at distances smaller than 20 kpc so, while the mass ratio is very similar, the tidal disturbance is smaller and the jump in A_2 is much less evident.

The A_2 coefficients start to grow for both galaxies after $z = 0.2$, $\sim$ 2 Gyr after the minor merger has ended (i.e. after $\sim$ 10 disk revolutions). In this period the instability grows at an accelerating pace. The growth has a markedly different time evolution with respect to the instability episode triggered by the minor merger. This suggests that the bar is due to the secular evolution of the disk. Moreover, the nice coincidence of the timing of bar growth at the two resolutions and the similar length of the resulting bar suggest that this instability is physical and not purely numerical, while the difference in bar strength is explained by the quick raise of the bar instability, so the GA1 at $z = 0$ happens to be caught at a higher A_2 value.

To investigate the physical cause of this bar instability, we consider two criteria commonly adopted in literature to assess when a disk is unstable to bar formation. The first one, proposed by Efstathiou et al. (1982) and based on N-body simulations, predicts that the regulator of bar instability is the relative contribution of the disk to the rotation curve:

$$\Upsilon_{\rm disk} = \frac{V_{\rm disk}}{\sqrt{G M_{\rm disk}/R_{\rm disk}}}\,, \qquad (10)$$

where, $M_{\rm disk}$, $R_{\rm disk}$ and $V_{\rm disk}$ are disk mass, radius and velocity respectively. Bar instability takes place whenever $\Upsilon_{\rm disk} \leqslant \epsilon_{\rm lim} \simeq 1$. To calculate this quantity, we use for $M_{\rm disk}$ the mass of galaxy particles within 10 kpc and with circularities $0.7 < \epsilon < 1.3$, for $R_{\rm disk}$ the half-mass radius of the same particles, and for $V_{\rm disk}$ the maximum of the galaxy rotation curve within 10 kpc. Results do not change if we use a different aperture to define disk mass and radius. Figure 11 shows the quantity $\Upsilon_{\rm disk}$ as a function of redshift, in both cases computed either using only star particles (blue lines) or all galaxy particles (red line). As usual, the left panel gives results for GA2, the right panel for GA1. The shaded regions denote values lower than a threshold $\epsilon_{\rm lim} = 1.1$ (Efstathiou et al. 1982) applying to a pure stellar disk, while a lower threshold of 0.9 has been suggested to apply to gas disks. As a result, although Υ decreases with time, it takes on values in any case above the suggested threshold.

The local stability of a self-gravitating disk to radial pertur-

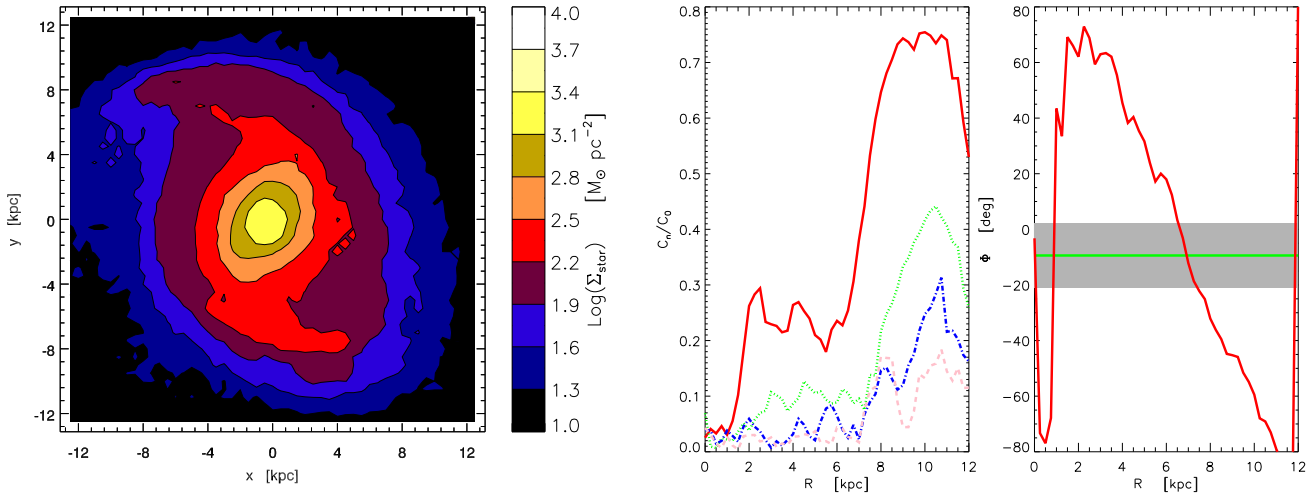

Figure 10. Stellar mass surface density maps (left panels), Fourier amplitudes (middle panel) and phase (right panel) for the GA2 galaxy at $z = 0.55$. Symbols and colors are like in Figures 3, 7 and 8.

bations is usually evaluated using the Toomre (1964) stability criterion. Though Toomre-unstable disks are expected to fragment into self-bound knots, a mildly unstable disk may develop a bar (Julian & Toomre 1966). Furthermore Athanassoula & Sellwood (1986) proposed that $Q > 2$ might be a general criterion against bar formation, since for these high Q values collective density waves become very weak and growth rates of all instabilities are reduced.

To compute the Toomre parameter of a two component disk (with stars and gas) we use, as in Monaco et al. (2012), the simplified approach of Wang & Silk (1994), that with high velocity dispersion approximates well the more accurate expression recently proposed by Romeo & Wiegert (2011), which is our case. We start from the separated component Q values:

$$Q_*(r) = \frac{\kappa\sigma_r}{3.36G\Sigma_*} \quad (11)$$

$$Q_g(r) = \frac{\kappa\sigma_r}{3.36G\Sigma_g} \quad (12)$$

where, for each component, $\Sigma(r)$ is its surface density, $\sigma_r(r)$ its radial velocity dispersion and $\kappa(r) = V(r)\sqrt{2 + 2d\ln V/d\ln r}/r$ the epicyclic frequency of the disk. The effective $Q_{\rm tot}(r)$ parameter of the disk is computed as:

$$Q_{\rm tot}(r) \simeq \left(\frac{1}{Q_g} + \frac{1}{Q_*}\right)^{-1} \quad (13)$$

Radial velocity dispersion is computed with the $3-\sigma$ rejection method described in Section 3.1, using as stellar surface density the one obtained rejecting $> 3-\sigma$ interlopers [3]. In all cases, we find that gas has a minor impact on $Q_{\rm tot}$. In fact, using Q_* alone would lead to the same conclusions.

Figure 12 shows $Q_{\rm tot}$ as a function of polar radius at redshift 0, 0.2, 0.6 and 1.0. Figure 13 shows $\langle Q\rangle$, the average value of $Q_{\rm tot}$ in the scale range from 3 to 8 kpc, computed for all available outputs of the two simulations at $z \leqslant 1$. In these plots the gray region denotes the $Q < 1$ values of the Toomre parameter where the disk is expected to be unstable. These galaxies are found to be formally stable at $z > 0.3$, but the Toomre parameter steadily decreases with time. From Figure 12 we see that, at $z = 0.6$, the disk of GA2 gets weakly unstable both at the center and at $\sim$ 6 kpc. As $z = 0.2$ this second instability region has got wider, while $\langle Q\rangle$ has got below the value of unity since $z \sim 0.3$. The GA1 galaxy becomes unstable at $r \sim 2$ and 6 kpc only at $z = 0.2$, but the evolution of $\langle Q\rangle$ is very similar to that of GA2. For both galaxies, the rise of the Toomre parameter at later time is due to the raise of σ_r, that is driven by the development of the radial streaming pattern.

Although the detailed behaviour of these galaxies is far from simple, the start of instability roughly coincides with the time when $\langle Q\rangle$ gets lower than the canonical threshold value of 1. Hence the behaviour of bar instability in these galaxies is consistent with the simple hypothesis that a bar is triggered by a secular instability.

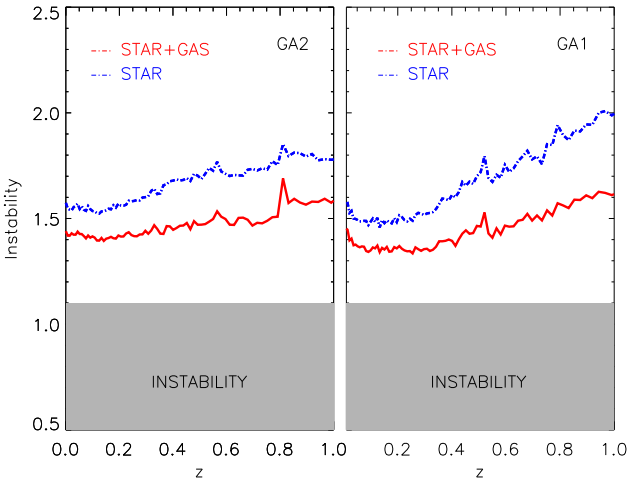

Figure 11. Υ_{disk} as a function of redshift for star particles (dot-dashed blue line) and for all galaxy particles (continuous red line); the shaded area marks the instability region corresponding to $\epsilon_{\rm lim} = 1.1$. Left panel: GA2; right panel: GA1.

[3] We report here that, with respect to the Gaussian fit, the $3-\sigma$ rejection method yields at the same time lower σ_r and lower $\Sigma_\star$ (Figure 1) and these corrections compensate in the value of $Q_\star$, that is then very insensitive to the method used.

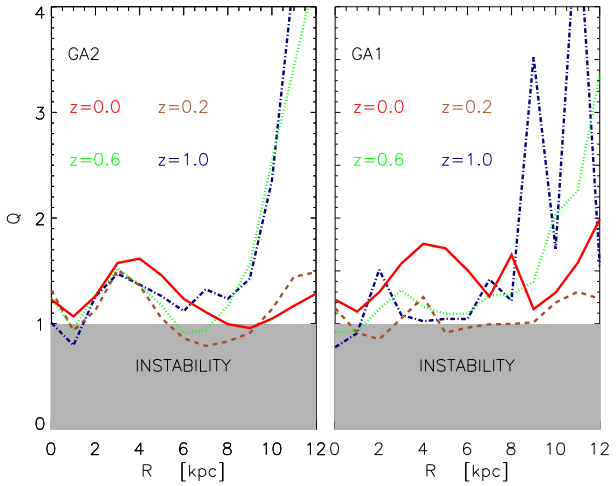

Figure 12. Toomre parameter $Q_{tot}(r)$ at $z = 0, 0.2, 0.6, 1.0$ (continuous red, dashed brown, dotted green and dot-dashed blue lines respectively). The shaded areas show the region where disk are formally unstable. Left panel: GA2; right panel: GA1.

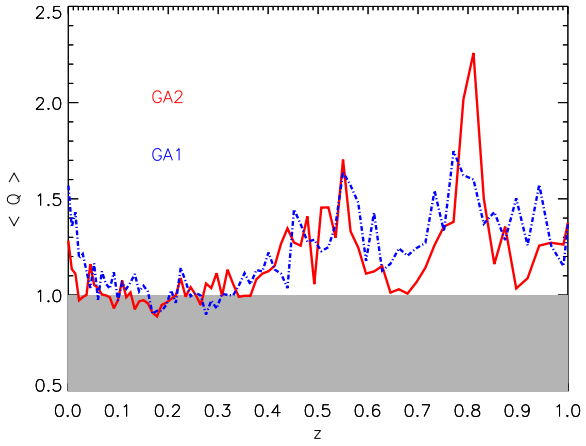

Figure 13. Average value of the Toomre parameter from 3 to 8 kpc, as a function of redshift, for GA1 (dot-dashed blue line) and GA2 (continuous red line). The shaded areas show the region where disks are formally unstable.

Assuming the validity of the criterion $\langle Q \rangle < 1$, the tidal disturbance at $z = 0.55$ takes place when the disk is still stable, while disk heating due to tidal interaction leads to an increase in velocity dispersion and therefore in $Q_{\rm tot}$ value. This may explain why the bar-like feature of GA2 is transient.

The reason for the late-time secular decrease of $Q_{\rm tot}$ towards the instability region is mostly due to the accumulation of the disk mass rather than to a variation of disk velocity dispersion. In Figure 14 we show the average disk radial velocity dispersion, stellar surface density and the ratio of the two. All quantities are evaluated in the range $3 \leqslant r \leqslant 8$ kpc and as a function of redshift. The radial velocity dispersion (top left of Figure 14) is boosted by the tidal interaction with the satellite and then it decreases before growing at $z \simeq 0.1$ in both GA1 and GA2, while stellar surface densities (top right of Figure 14) increase always with time. Accordingly, their

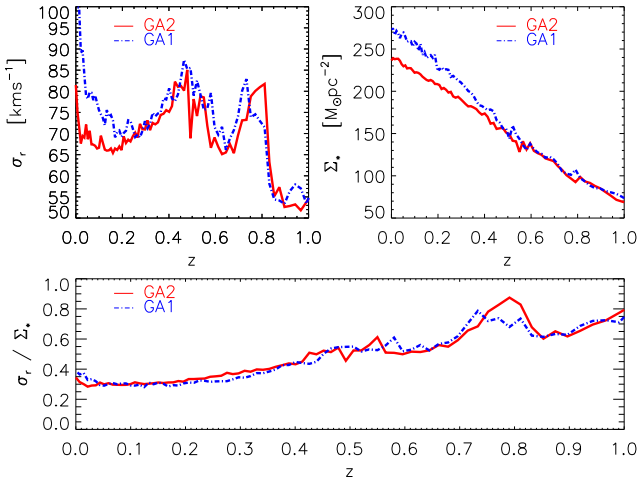

Figure 14. Disk radial velocity dispersion (top left panel), stellar disk surface density (top right panel) and their ratio as a function of redshift (bottom panel). All these quantities are averaged from 3 to 8 kpc. Continuous red line for GA2 and dot-dashed blue line for GA1.

ratio decreases with time (bottom panel of Figure 14). This demonstrates that the decrease of $Q_{\rm tot}$, that is the most likely cause of the bar, is the accumulation of the disk mass at low redshift, due to the continuous infall of gas into the DM halo.

3.6 The role of halo triaxiality

As mentioned in the introduction, halo triaxiality is a potential trigger of bar instability, though the precise role of triaxiality has been debated in the papers discussed above. In those papers, halos were extracted from collisionless N-body simulations and disks were placed inside them. As a matter of fact, this implies that the gravitational influence that the formation of the disk has had on the structure of the halo itself is neglected. The impact of the formation of a gaseous disk on the shape of a dark matter halo and its transformation from prolate to oblate in the inner part was already studied in isolated systems by Dubinski (1994), Debattista et al. (2008), in cosmological environment by Kazantzidis et al. (2004), Tissera et al. (2010), Abadi et al. (2010) and more recently by Zemp et al. (2012), Bryan et al. (2013). DeBuhr et al. (2012) inserted live stellar disks inside Milky Way-like dark matter halos from the Aquarius simulations, finding a strong effect on the shapes of the inner halos which evolve to become oblate.

In our paper I we have shown that, consistently with many other papers (e.g. Governato et al. 2012), the inner slope of the dark matter halo of our GA2 simulation is flatter than the typical $\rho \propto r^{-1}$ slope obtained when particles are collisionless. This is due to the combined action of the adiabatic contraction caused by the formation of the galaxy and the violent expansion due to episodic massive outflows. The same process induces changes in the DM distribution in the region occupied by the galaxy.

To address the influence that the formation of the galaxy has on the inner regions of the DM halo, we performed a simulation of the GA2 switching off hydrodynamics, cooling and star formation, thus treating both DM and gas particles as collisionless particles; we will call it GA2-cless in the following. For the GA2 and GA2-cless simulations we compute the inertia tensor of all DM particles within a distance of $r_{200}/10$ (30.64 kpc for GA2-cless,

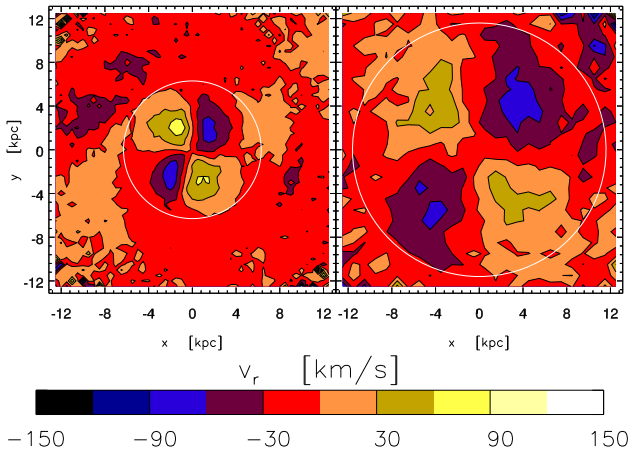

Figure 16. As in Figure 6: radial velocity maps on edge-on views of the two simulated AqC5 (left panel) and AqC6 (right panel) galaxies. The white circle marks the bar length L_{bar}.

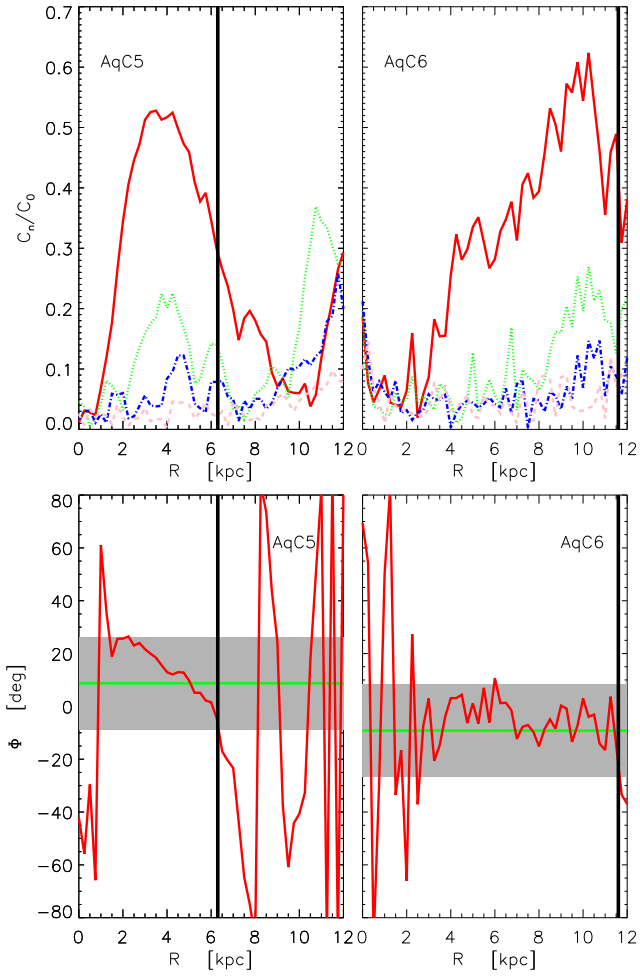

Figure 17. As in Figure 7 and 8: Fourier analysis of the AqC5 (left panels) and AqC6 (right panels) galaxies. Upper panels show the amplitude of even Fourier coefficients, the lower panels the phase of C_2. The black lines mark the bar length L_{bar}.

29.98 kpc for GA2) and quantify the ratios among the eigenvalues I_i (with $i = 1, 2, 3$), ranked in decreasing order. In GA2-cless we find $I_1/I_2 = 1.07$, $I_1/I_3 = 1.39$ and $I_2/I_3 = 1.30$, indicating a roughly prolate shape with significant triaxiality. In GA2, where the DM halo has hosted a forming spiral galaxy, the ratios of eigenvalues are $I_1/I_2 = 1.13$, $I_1/I_3 = 1.14$ and $I_2/I_3 = 1.01$, indicating an oblate and nearly axisymmetric shape. Moreover, the eigenvector corresponding to the largest eigenvalue of the inertia tensor, i.e. to the direction where the halo is flattened, is found to be aligned with the galaxy angular momentum within 4.37°. This alignment allows to infer that the oblate shape is due to the formation of the disk itself.

We conclude that the influence of the triaxiality on disk dynamics should not be addressed without considering, at the same time, the influence that astrophysical processes bringing to disk formation have on the triaxiality of the inner part of the DM halo.

4 THE AQ5 AND AQ6 GALAXIES

The two AqC simulations show a different behaviour with respect to the GA ones. Here we show the surface density maps (Figure 15), the face-on map of radial velocities (Figure 16), the Fourier coefficients and phases (Figure 17) and the evolution of A_2 and $\langle Q \rangle$, the latter being averaged again on $3 < r < 8$ kpc (Figure 18). The higher resolution AqC5 galaxy at $z = 0$ has a bar with properties similar to the one of GA2 (Figure 15), visible as an elongation of the isodensity contours, but with a slightly smaller size with respect to the GA galaxies (Figure 15). The signature of streaming motions very clearly confirms the visual impression (Figure 16). The Fourier analysis (Figure 17) confirms the presence of a bar with maximal amplitude of $C_2/C_0 \sim 0.5$ at ~ 4 kpc and a bar length of $L_{\rm bar} = 6.3$ kpc. Spiral arms here give a much smaller contribution to the amplitude of the $m = 2$ mode.

The origin of this bar is however different: in Figure 18 we see that the A_2 coefficient starts to increase at $z \sim 0.6$, while the disk is stable according to $\langle Q \rangle$. As mentioned in Section 2, this galaxy happens to suffer a minor merger at roughly the same time as the GA galaxy. In particular, at $z = 0.52$, the galaxy suffers a near passage at ~ 20 kpc of a 1.6×10^9 M$_\odot$ satellite, with a mass ratio of $1 : 32$ with respect to the main galaxy. Further near passages are at $z = 0.43$ and $z = 0.35$, when the satellite gets tidally destroyed. These times are reported in Figure 18 as vertical black lines. This coincides with the time interval where the A_2 coefficient increases from ~ 0.05 to ~ 0.17 and it supports the idea that this bar is triggered by a tidal interaction. The main difference with respect to the GA galaxy lies in the higher mass ratio, though the merger is still considered minor.

The AqC6 galaxy behaves differently. Analogously to the GA simulations, the perturbation from the satellite does not trigger a bar. Indeed, the dynamics of the merger is different in this case: the satellite suffers a much slower orbital decay, so that the apocenter of the orbit is still ~ 30 kpc at $z = 0.45$. The nearest encounter, at 19 kpc, is found only at $z = 0.24$, while the tidal disruption takes place at $z = 0.14$. At such late times the $Q_{\rm tot}$ parameter is close to 1 and the A_2 coefficient starts to raise again as in the GA case. While the cause in this case seems to be the disk secular evolution (driven by the progressive accumulation of the disk mass, as in Figure 14), we cannot exclude that the bar is tidally triggered.

Figures 15, 16 and 17 show that in this case the bar-like

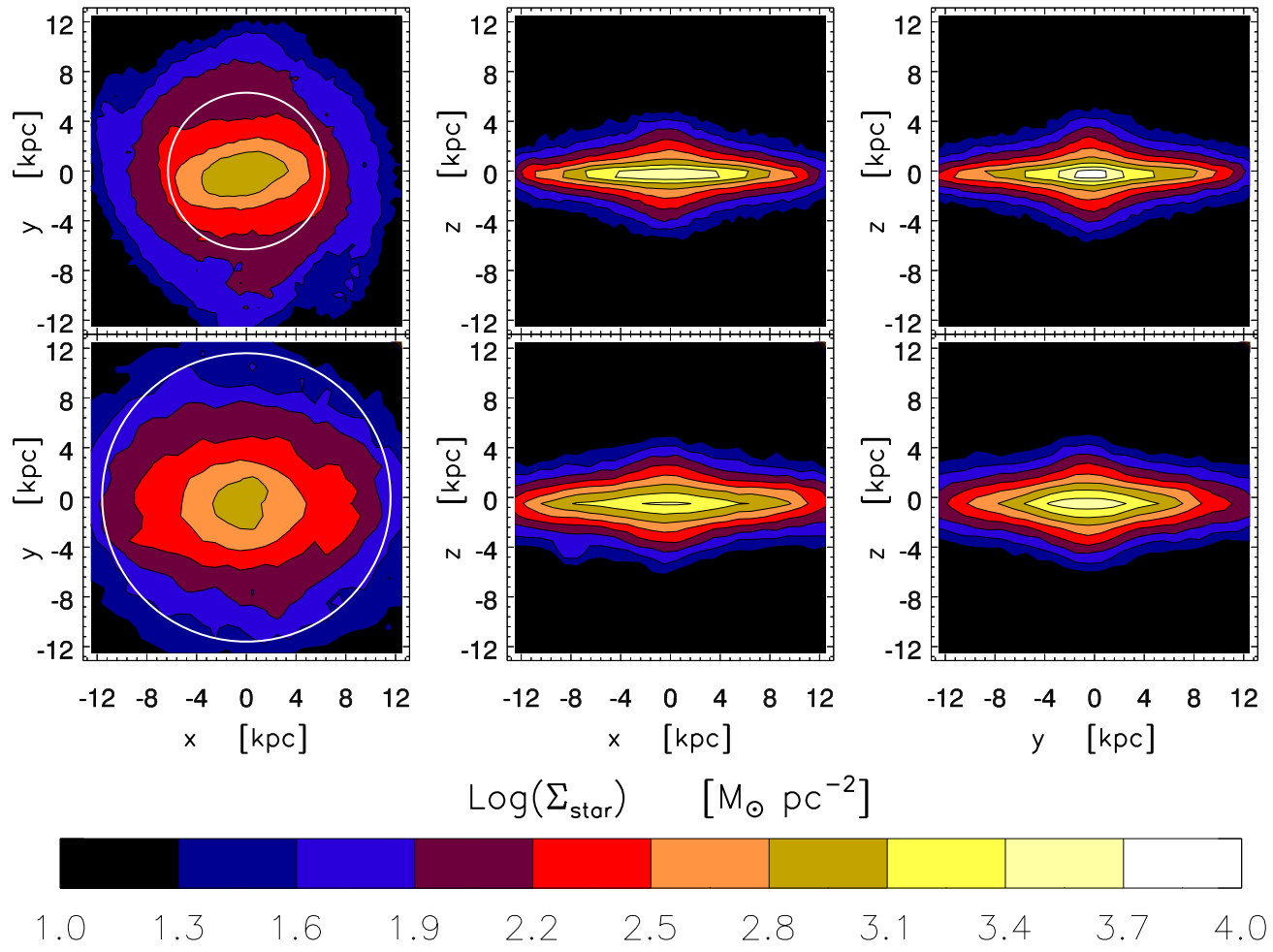

Figure 15. As in Figure 3: projected stellar maps of the AqC5 (top panels) and AqC6 (bottom panels) galaxies at $z = 0$. The white circle marks the bar length L_{bar}.

signatures in streaming motions and Fourier analysis are relatively strong, but the bar is very long, with an estimated length of $L_{\rm bar} = 11$ kpc and the isodensity contours are not very flattened. The galaxy appears to be caught during the early development of a very strong and long bar.

5 CONCLUSIONS

In paper I we showed results of simulations of disk galaxies in $\sim 2 - 3 \times 10^{12}$ M$_\odot$ halos, using two sets of initial conditions (GA, Stoehr et al. (2002) and AqC, Springel et al. (2008), Scannapieco et al. (2009)) at two resolutions. In all cases, extended disks were obtained with low B/T ratios and general properties (disk size, mass surface density, rotation velocity, gas fraction) that are consistent with observations of the local universe. These galaxies develop a bar at low redshift, which is still consistent with the relatively high fraction (~ 60 per cent) of bars found in such massive spiral galaxies. In this paper we quantified the properties of these bars, starting from morphology and kinematics of the inner region of the galaxies, then performing a Fourier analysis of the mass surface density map to assess the strength and length of the bars. We investigated the physical conditions that cause bar instability and found that a combination of low values of Toomre parameters and minor mergers can explain the emergence of bars in our simulations.

Our main conclusions are the following:

(i) The close similarity of bar properties at $z = 0$ and of the development of the instability at $z \leqslant 0.3$ for GA2 and GA1, which differ in mass resolution by a factor of 9.3, disfavors the hypothesis that these bars are a result of a numerical instability due to poor resolution.

(ii) Despite the softening does not allow to properly resolve the vertical structure of the disk, we find our simulated disks to have vertical and radial velocity dispersion compatible with observations, at least for $r < 10$ kpc.

(iii) In the GA simulations the morphology and kinematics of the inner ~ 10 kpc are fully consistent with the presence of a bar. In both cases the typical kinematic signatures of increased line-of-sight velocity dispersion and radial streaming motions are present. The Fourier analysis shows that C_2/C_0 peaks to values of 0.4 and 0.7 in the GA2 and GA1 cases, that the bar length is $L_{\rm bar} \simeq 8.8$ kpc in both cases.

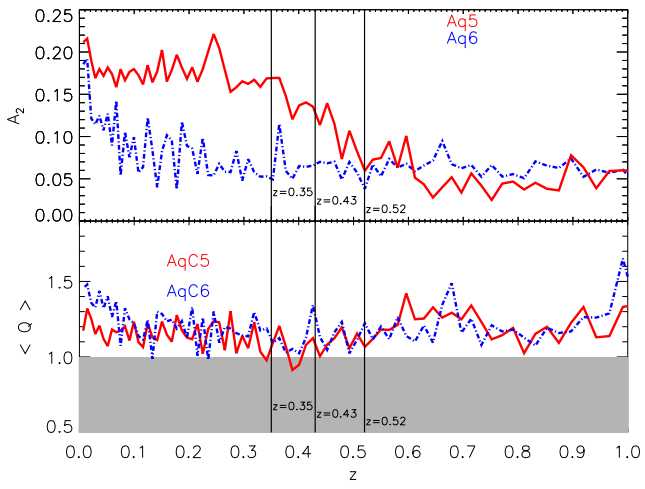

Figure 18. As in Figures 9 and 13: evolution with redshift of A_2 (upper panel) and $\langle Q \rangle$ (lower panel) for the AqC5 (continuous red lines) and AqC6 (dot-dashed blue lines). Vertical lines give the times of near passages and final merger of the satellite.

(iv) The time evolution of A_2 shows that this instability starts at $z = 0.2$ and quickly rises at $z = 0$ for both GA2 and GA1, so the difference in bar strength is likely due to a small time offset in the growth of the structure.

(v) Before the onset of bar instability, disks result to be stable according to the criterion proposed by Efstathiou et al. (1982) and they are very close to the threshold of Toomre instability, with $Q_{\rm tot} \simeq 1$.

(vi) A minor merger taking place from $z = 0.57$ to $z = 0.35$, with a stellar mass ratio of $1 : 50$, results, especially in GA2, in a transient tidal disturbance with high values of the A_2 coefficient which disappears as quickly as it has appeared. A Fourier analysis reveals that the perturbation is due to a strong spiral pattern rather than to a bar.

(vii) The AqC simulations follow a different path. At a higher resolution (AqC5), a minor merger taking place from $z = 0.52$ to $z = 0.35$ induces a true bar that lasts until the end of the simulation. The $\langle Q \rangle$ parameter is greater than 1 before the first close encounter with the satellite, but the mass ratio is higher in this case ($1 : 32$) and this likely justifies the different behaviour of AqC5 with respect to GA2. The final bar has a length of $L_{\rm bar} = 6.5$ kpc.

(viii) The minor merger in AqC6 takes place at later times. In this case the disk gets barred in a way similar to the GA galaxy. However, in this case the role of the merger in the triggering of the bar cannot be excluded. The resulting bar is very long ($L_{\rm bar} = 11$ kpc) and it is caught in a relatively early phase of development.

(ix) We find that the formation of the disk influences the triaxiality of the inner regions of the DM halo. In the GA2-cless simulation, performed treating both DM and gas particles as collisionless particles, the DM halo is triaxial, while in GA2, where the halo has hosted the formation of a spiral galaxy, the inertia tensor of the DM halo is roughly oblate and its eigenvector corresponding to the largest eigenvalue is found to be well aligned with the galaxy angular momentum. Thus, special care is needed in addressing the role of triaxiality on bar instability when disks are embedded in DM halos extracted from collisionless simulations.

Overall, our simulations are consistent with a relatively simple picture of bar instability being triggered either by secular processes in Toomre-unstable disks ($Q_{\rm tot} \lesssim 1$) or by minor mergers, when the stellar mass ratio is at least of order $1 : 30$. With mass ratios as small as $1 : 50$, the merger can stimulate transient features that may look like bars but do not pass a test based on Fourier phases. Of course, these simulations do not give sufficient statistics to provide this picture with the proper justification. We tested several versions of our code on these sets of IC and we noticed that bars may or may not come out, depending on the detailed state of the galaxy. For instance, the AqC5 galaxy in the Scannapieco et al. (2012) paper, run with a previous version of our code with pure thermal feedback, primordial cooling and no chemical evolution, showed a very strong bar (the whole disk had collapsed into a cigar-like structure). A similar thing happens to GA2 when simulated with the same code. In this two cases we found that the bar is triggered by the two minor mergers discussed above, while the disks are Toomre-stable before the merger. The difference in this case is that, due to the fact that feedback is less effective in limiting star formation in small halos, mass ratios are much larger.

As a concluding remark, our results are found to be stable with resolution at least in the GA case, hence we consider the origin of the bar physical rather than purely numerical. However, the presence of a bar depends on the fine details of the disk structure and its environment that are not yet numerically under full control, as the different timing of the satellite merging in AqC5 and AqC6 testifies. So these results are not a premise to a robust prediction of the presence of bars in simulated disks, but it will certainly allow to better understand the emergence of this complex phenomenon that, although it has been observed since the beginning of extragalactic astronomy, is still not well understood.

ACKNOWLEDGMENTS

We thank Volker Springel who provided us with the non-public version of the GADGET-3 code. We acknowledge useful discussions with Stefano Borgani, Gabriella De Lucia, Emiliano Munari and Marianna Annunziatella. The simulations were carried out at the "Centro Interuniversitario del Nord-Est per il Calcolo Elettronico" (CINECA, Bologna), with CPU time assigned under University-of-Trieste/CINECA and ISCRA grants, and at the CASPUR computing center with CPU time assigned under two standard grants. This work is supported by the PRIN MIUR 2010-2011 grant "The dark Universe and the cosmic evolution of baryons: from current surveys to Euclid", by the PRIN-MIUR 2012 grant "Evolution of Cosmic Baryons", by the PRIN-INAF 2012 grant "The Universe in a Box: Multi-scale Simulations of Cosmic Structures", by the INFN "INDARK" grant, by the European Com- missions FP7 Marie Curie Initial Training Network CosmoComp (PITN-GA-2009-238356), by the FRA2012 grant of the University of Trieste and by "Consorzio per la Fisica di Trieste".

REFERENCES

Abadi M. G., Navarro J. F., Fardal M., Babul A., Steinmetz M., 2010, MNRAS, 407, 435
Abadi M. G., Navarro J. F., Steinmetz M., Eke V. R., 2003, ApJ, 597, 21
Aguerri J. A. L., Beckman J. E., Prieto M., 1998, AJ, 116, 2136
Aguerri J. A. L., Debattista V. P., Corsini E. M., 2003, MNRAS, 338, 465
Athanassoula E., 2005, MNRAS, 358, 1477

Athanassoula E., Machado R. E. G., Rodionov S. A., 2013, MNRAS, 429, 1949
Athanassoula E., Misiriotis A., 2002, MNRAS, 330, 35
Athanassoula E., Sellwood J. A., 1986, MNRAS, 221, 213
Aumer M., White S. D. M., Naab T., Scannapieco C., 2013, MNRAS, 434, 3142
Barazza F. D., Jogee S., Marinova I., 2008, ApJ, 675, 1194
Berentzen I., Shlosman I., Jogee S., 2006, ApJ, 637, 582
Bosma A., 1978, PhD thesis, PhD Thesis, Groningen Univ., (1978)
Bryan S. E., Kay S. T., Duffy A. R., Schaye J., Dalla Vecchia C., Booth C. M., 2013, MNRAS, 429, 3316
Buta R., Laurikainen E., Salo H., Block D. L., Knapen J. H., 2006, AJ, 132, 1859
Combes F., Elmegreen B. G., 1993, A&A, 271, 391
Curir A., Mazzei P., 1999, A&A, 352, 103
Curir A., Mazzei P., Murante G., 2006, A&A, 447, 453
Curir A., Mazzei P., Murante G., 2007, A&A, 467, 509
Curir A., Mazzei P., Murante G., 2008, A&A, 481, 651
Debattista V. P., Mayer L., Carollo C. M., Moore B., Wadsley J., Quinn T., 2006, ApJ, 645, 209
Debattista V. P., Moore B., Quinn T., Kazantzidis S., Maas R., Mayer L., Read J., Stadel J., 2008, ApJ, 681, 1076
Debattista V. P., Sellwood J. A., 1996, ArXiv Astrophysics e-prints
Debattista V. P., Sellwood J. A., 2000, ApJ, 543, 704
DeBuhr J., Ma C.-P., White S. D. M., 2012, MNRAS, 426, 983
Dubinski J., 1994, ApJ, 431, 617
Dubinski J., Gauthier J.-R., Widrow L., Nickerson S., 2008, in Funes J. G., Corsini E. M., eds, Formation and Evolution of Galaxy Disks Vol. 396 of Astronomical Society of the Pacific Conference Series, Spiral and Bar Instabilities Provoked by Dark Matter Satellites. p. 321
Efstathiou G., Lake G., Negroponte J., 1982, MNRAS, 199, 1069
Elmegreen B. G., Elmegreen D. M., 1985, ApJ, 288, 438
Eskridge P. B., Frogel J. A., Pogge R. W., Quillen A. C., Davies R. L., DePoy D. L., Houdashelt M. L., Kuchinski L. E., Ramírez S. V., Sellgren K., Terndrup D. M., Tiede G. P., 2000, AJ, 119, 536
Fall S. M., Efstathiou G., 1980, MNRAS, 193, 189
Gadotti D. A., 2011, MNRAS, 415, 3308
Governato F., Willman B., Mayer L., Brooks A., Stinson G., Valenzuela O., Wadsley J., Quinn T., 2007, MNRAS, 374, 1479
Governato F., Zolotov A., Pontzen A., Christensen C., Oh S. H., Brooks A. M., Quinn T., Shen S., Wadsley J., 2012, MNRAS, 422, 1231
Guedes J., Callegari S., Madau P., Mayer L., 2011, ApJ, 742, 76
Guedes J., Mayer L., Carollo M., Madau P., 2013, ApJ, 772, 36
Julian W. H., Toomre A., 1966, ApJ, 146, 810
Kazantzidis S., Kravtsov A. V., Zentner A. R., Allgood B., Nagai D., Moore B., 2004, ApJ, 611, L73
Kormendy J., 1982, ApJ, 257, 75
Kormendy J., Kennicutt Jr. R. C., 2004, ARAA, 42, 603
Kraljic K., Bournaud F., Martig M., 2012, ApJ, 757, 60
Leroy A. K., Walter F., Brinks E., Bigiel F., de Blok W. J. G., Madore B., Thornley M. D., 2008, AJ, 136, 2782
Marinacci F., Pakmor R., Springel V., 2013, MNRAS
Michel-Dansac L., Wozniak H., 2006, A&A, 452, 97
Monaco P., Murante G., Borgani S., Dolag K., 2012, MNRAS, 421, 2485
Murante G., Monaco P., Borgani S., Tornatore L., Dolag K., 2014, submitted to MNRAS
Murante G., Monaco P., Giovalli M., Borgani S., Diaferio A., 2010, MNRAS, 405, 1491
Navarro J. F., Frenk C. S., White S. D. M., 1996, ApJ, 462, 563
Noguchi M., 1996, ApJ, 469, 605
Ohta K., 1996, in Buta R., Crocker D. A., Elmegreen B. G., eds, IAU Colloq. 157: Barred Galaxies Vol. 91 of Astronomical Society of the Pacific Conference Series, Global Photometric Properties of Barred Galaxies. p. 37
Ohta K., Hamabe M., Wakamatsu K.-I., 1990, ApJ, 357, 71
Okamoto T., 2013, MNRAS, 428, 718
Okamoto T., Isoe M., Habe A., 2014, ArXiv e-prints
Ostriker J. P., Peebles P. J. E., 1973, ApJ, 186, 467
Romeo A. B., Wiegert J., 2011, MNRAS, 416, 1191
Scannapieco C., Athanassoula E., 2012, MNRAS, 425, L10
Scannapieco C., Tissera P. B., White S. D. M., Springel V., 2006, MNRAS, 371, 1125
Scannapieco C., Tissera P. B., White S. D. M., Springel V., 2008, MNRAS, 389, 1137
Scannapieco C., Wadepuhl M., Parry O. H., Navarro J. F., Jenkins A., Springel V., Teyssier R., Carlson E., Couchman H. M. P., Crain R. A., Dalla Vecchia C., Frenk C. S., Kobayashi C., et al., 2012, MNRAS, 423, 1726
Scannapieco C., White S. D. M., Springel V., Tissera P. B., 2009, MNRAS, 396, 696
Sellwood J. A., Nelson R. W., Tremaine S., 1998, ApJ, 506, 590
Springel V., 2005, MNRAS, 364, 1105
Springel V., Wang J., Vogelsberger M., Ludlow A., Jenkins A., Helmi A., Navarro J. F., Frenk C. S., White S. D. M., 2008, MNRAS, 391, 1685
Springel V., White S. D. M., Tormen G., Kauffmann G., 2001, MNRAS, 328, 726
Stinson G. S., Bovy J., Rix H.-W., Brook C., Roškar R., Dalcanton J. J., Macciò A. V., Wadsley J., Couchman H. M. P., Quinn T. R., 2013, MNRAS, 436, 625
Stoehr F., White S. D. M., Tormen G., Springel V., 2002, MNRAS, 335, L84
Teyssier R., 2002, A&A, 385, 337
Tissera P. B., White S. D. M., Pedrosa S., Scannapieco C., 2010, MNRAS, 406, 922
Toomre A., 1964, ApJ, 139, 1217
Tornatore L., Borgani S., Dolag K., Matteucci F., 2007, MNRAS, 382, 1050
Wang B., Silk J., 1994, ApJ, 427, 759
White S. D. M., Rees M. J., 1978, MNRAS, 183, 341
Wiersma R. P. C., Schaye J., Theuns T., Dalla Vecchia C., Tornatore L., 2009, ArXiv e-prints
Zemp M., Gnedin O. Y., Gnedin N. Y., Kravtsov A. V., 2012, ApJ, 748, 54